

# **DEVELOPMENT OF FINITE ELEMENT MODEL OF A PENTAMODE STRUCTURE FOR PREDICTING THE COMPRESSIVE MECHANICAL BEHAVIOUR INCORPORATING MACHINE LEARNING AND POROUS PLASTICITY MODELS**

Mohammed, Asif, Kolasangiani, Kamal, Nayyeri, Pooyan, Oguamanam, Donatus and Bougherara, Habiba\*

Department of Mechanical, Industrial, and Mechatronics Engineering, Toronto Metropolitan University, Toronto, Canada

\* Corresponding author (habiba.bougherara@torontomu.ca)

**Keywords:** *Pentamode Structures; Finite Element Modeling; Machine Learning*

## **Abstract**

Pentamode structures are valued for their versatility, strength-to-weight ratio, and ability to be engineered for specific mechanical and acoustic properties. They are utilized in biomedical applications, such as prostheses, stents, and scaffolds, as well as in mechanical applications, such as energy absorption, vibration, and insulation. In this paper, the compressive mechanical behaviour of pentamode specimens is experimentally and numerically investigated. Pentamode specimens were fabricated from polylactic acid using stereolithographic 3D printing method and were tested using an Instron test frame. Finite element (FE) analysis, incorporating Armstrong-Friedrich and Gurson-Tvergaard-Needleman models, was used to predict the elastoplastic and damage behaviour of the pentamode structure. The parameters of the finite element model were obtained from tensile test results and Machine Learning techniques. The FE results showed good agreement with experimental data in the elastoplastic region; however, the model was less accurate in predicting the damage region.

## **1. Introduction**

Additive manufacturing (AM) has significantly transformed the landscape of material science and engineering, enabling the fabrication of complex structures with precision and efficiency. Stereolithography (SLA) technique can process parts with layer thickness of the order of 10  $\mu\text{m}$  allowing intricate and small part geometries being fabricated with reasonable accuracy. Photosensitive polymers in liquid resins are cured a layer at a time in the SLA technique. Polylactic acid (PLA) is a widely available and low cost material for SLA. PLA with SLA technique has been used in [1] and [2] to manufacture auxetic materials. Other studies involving PLA with different AM methods are reported in [3] and [4]. To manufacture functional components via AM, it is necessary to know the mechanical behaviour of the 3D material under different stress states and strain rates. Finite element (FE) models can provide detailed insight on the mechanical behaviours demonstrated in [5]-[8].

The study reported herein is an attempt to predict the compressive behaviour of two pentamode structures using FE analysis. To develop the FE model to capture the behaviour of the PLA, the Armstrong-Friedrich (AF) and Gurson-Tvergaard-Needleman (GTN) model parameters were calibrated using tensile test results and supervised machine learning (ML). The FE model was then used to simulate compression tests of the pentamode structures, and the results were compared to the experimental results to assess the effectiveness of the model in predicting the elastoplastic and damage responses of the two pentamode structures.

## 2. Material and Methods

### 2.1 Material and Manufacturing

Commercially available gray PLA resin from Shenzhen eSun Industrial Co., Ltd. was used in the SLA printing process. Urethane acrylate and Epoxy acrylate are the prepolymers in this resin, 2-Phenoxyethyl acrylate and 1,6-Hexanediol diacrylate are the diluents, while Trimethyl- benzoyl-diphenyl phosphine oxide is the photoinitiator. A Standard Tessellation Language (STL) file of each pentamode model was generated using Solidworks CAD models and imported into the slicing software to generate the 2D layers that are usable in AM. A Flashforge Foto 13.3 SLA printer with 4K HD resolution was used to 3D print the pentamodes with layer height of 30  $\mu\text{m}$ . The UV exposure time per layer was 6 seconds.

ASTM D638 Type I tensile test specimens were printed in vertical and horizontal orientations (see Figure 1) to check for anisotropy. The pentamodes were added with a bottom plate and four scaffolds to support the struts on the edge by the slicing software. The printed samples were initially introduced into a Monocure 3D Resinway® UV resin cleaning solution bath for 5 minutes to separate non-cured traces of resin from the sample, followed by washing and drying completely, and finally post-curing by UV exposure for 5 minutes to harden the specimen by increasing the degree of polymerization and generate polymer chain cross-linking.

### 2.2 Mechanical Tests and SEM characterization

Tensile tests were conducted on the ASTM D-638 Type I specimens using a servo-hydraulic MTS 370 (Eden Prairie, MN, USA) test frame with hydraulic grips. Three vertically fabricated and three horizontally fabricated specimens were tested at a displacement rate of 2 mm/min. A clip-on extensometer with a gauge length of 25.4 mm was used to measure the axial strain. The load and strain data were then used to determine the Young's modulus, yield point, ultimate strength, and failure strain. Compressive tests of the PLA pentamodes were performed using an Instron 68TM30 with static force calibration conforming to ASTM E4 (see Figure 2(a)). A displacement rate of 5 mm/min was used on the crosshead carrying the top plate with the specimen centrally positioned on the bottom plate. The plates are made of stainless steel.

To apply the GTN porous failure criteria, it is essential to have the initial void volume fraction (VVF) for the virgin specimen. Hence, a Hitachi Flex SEM 1000II Scanning Electron Microscope was used to obtain SEM images. As reported in [3] and [8], Backscattered Electron imaging technique at 50 Pa pressure applying an electron accelerating voltage of 5 kV from 4.7 mm distance with 1990 times magnification revealed the presence of voids and cracks (see Figure 2(b)). Factors such as trapped air bubbles, inadequate resin flow, and improper curing at layer interfaces could result in the formation of such defects. An image analysis for calculating the VVF was implemented using Image J software.

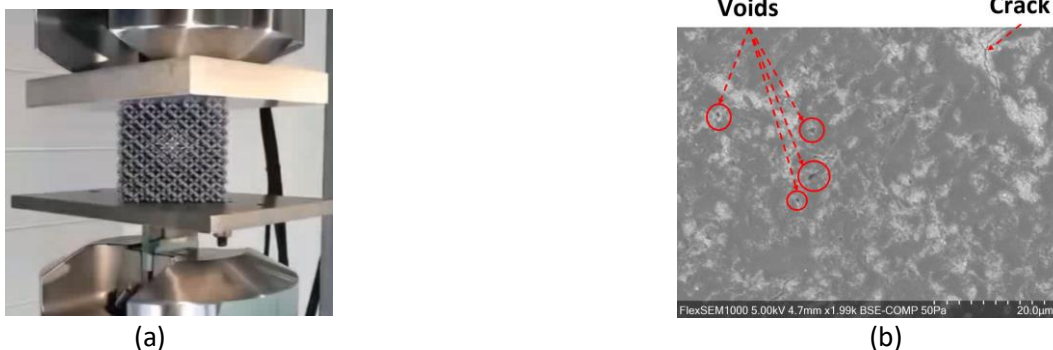


Figure 2. (a) Pentamode compression test setup; (b) SEM image showing voids in printed virgin PLA

### 2.3 Machine Learning Model

Machine learning (ML) algorithms based on regression learner toolbox in MATLAB were trained to optimize the parameters of the AF and GTN models used for the plastic and the damage regions respectively [3]. The constitutive model parameters to be optimized are  $C, \gamma, f_N, f_C, f_F, \varepsilon_N, S_N$ . The governing equations involving these parameters are described in Eqs. (1)-(5) as follows:

Armstrong-Friedrich (AF):

$$\sigma_x = \frac{C}{\gamma} \left[ 1 - e^{-\gamma \varepsilon_x^{pl}} \right] + \sigma_{y0} \quad (1)$$

where  $\sigma_x$  is the plastic stress,  $\sigma_{y0}$  is the initial yield stress,  $\varepsilon_x^{pl}$  is the plastic strain starting with a zero value at the yield point,  $C$  is the linear kinematic hardening modulus, and  $\gamma$  is a parameter that determines the rate at which the kinematic hardening modulus decreases with increasing plastic deformation.

Gurson-Tvergaard-Needleman (GTN) Yield function:

$$g(\sigma_{eq}, \sigma_m, \sigma_y, f^*) = \left( \frac{\sigma_{eq}}{\sigma_y} \right)^2 + 2q_1 f^* \cosh\left(\frac{3}{2} \cdot q_2 \cdot \frac{\sigma_m}{\sigma_y}\right) - 1 - q_3 f^{*2} = 0 \quad (2)$$

where  $\sigma_m$  is the hydrostatic stress component of the Cauchy stress tensor,  $\sigma_{eq} = \sqrt{\frac{3}{2} \cdot S_{ij} \cdot S_{ij}}$  is the von Mises equivalent stress where  $S_{ij}$  is the deviatoric stress component of the Cauchy stress tensor,  $\sigma_y$  is the yield stress of the matrix material without pores,  $q_1, q_2,$  and  $q_3$  are the yield function coefficients, and  $f^*$  is the void volume fraction.

Void Volume Fraction (VVF):

$$f^* = \begin{cases} f & \text{if } f^* \leq f_C \\ f_C + \frac{f_U - f_C}{f_F - f_C} (f - f_C) & \text{if } f_C < f^* \leq f_F \end{cases} \quad (3)$$

$$f_U = \frac{q_1 + \sqrt{q_1^2 - q_3}}{q_3}$$

where  $f^*$  is the void volume fraction,  $f_C$  is the critical void fraction,  $f_F$  total void fraction at failure,  $f_U$  is the ultimate value of the void volume fraction at which the stress carrying capacity is zero ( $\sigma_m = 0, \sigma_{eq} = 0$ ) and  $f^* = f_F$ , and  $f_N$  is the nucleated void volume fraction. The nucleated void volume fraction,  $f_N$ , is related to both the mean void nucleation strain,  $\varepsilon_N$ , and the standard deviation of the mean void nucleation strain,  $S_N$ , via Eqs. (4) and (5):

$$df_{nucleation} = A \cdot d\varepsilon_m^{pl} \quad (4)$$

$$A = \frac{f_N}{S_N \sqrt{2\pi}} \exp\left[-\frac{1}{2} \left(\frac{\varepsilon_m^{pl} - \varepsilon_N}{S_N}\right)^2\right] \quad (5)$$

A typical force-displacement curve of the tensile specimen is depicted in Figure 3, showing the overall agreement between experimental results and FE model with optimized parameters [9].

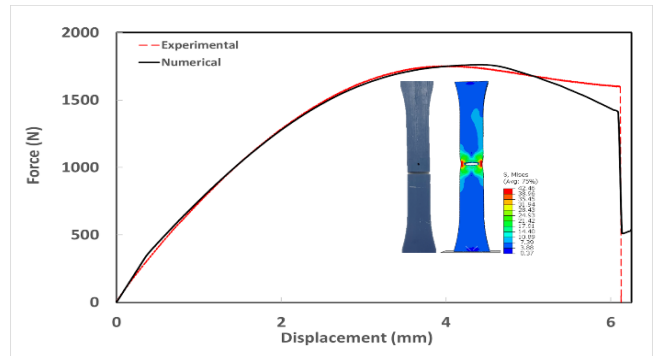


Figure 3. Force vs. displacement curve of ASTM D638 tested coupon and optimized FE model.

## 2.4 Finite Element Analysis

The 3D geometry of the pentamode structure was generated in Solidworks and were constructed from unit cells having body-centered cubic arrangement of tetrahedrally oriented four symmetric double cone elements. Two configurations (labelled as 4d and 5d) were evaluated. Configuration 4d has cone apex diameter and a cone base diameter of  $d = 0.70$  mm and  $D = 2.8$  mm, while configuration 5d has a cone apex diameter  $d = 0.70$  mm and a cone base diameter  $D = 3.5$  mm. The 3D geometry of the two configurations were then imported into Abaqus for analysis. The boundary conditions used in the FE model are similar to those of the experimental testing (see Figure 4). A mesh sensitivity was conducted and a global mesh size of 0.3 mm with a  $1 \times 10^{-6}$ s time increment were sufficient for convergence.

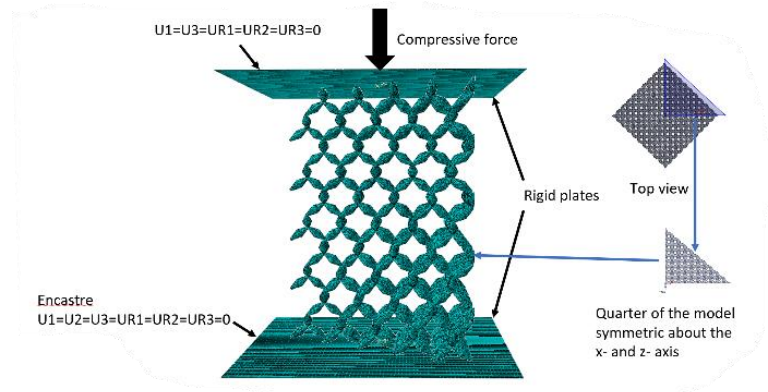


Figure 4. Finite element model.

## 3. Results and discussion

Figure 5 illustrates the force-displacement curves for each of the three specimens with 5d and 4d configurations. All the 5d specimens exhibit higher stiffness compared to the 4d specimens, which is in agreement with results reported in [2]. The maximum forces withstood by the 5d specimens were also higher than those by 4d. This is because the greater overlap at the strut joints in 5d specimens due to their thicker struts caused them to have more material compared to the joints of the 4d specimens. The struts in 5d specimens were also allowed less deformation under same load.

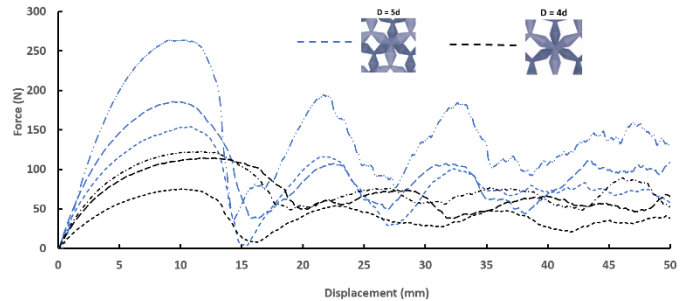


Figure 5. Experimental results showing the force vs displacement for the two pentamode configurations.

The peaks and troughs forming the humps in the force-displacement curves indicate the failure of layers in the pentamodes [10], [11]. The troughs after the failure of the first layers in 5d specimens were around 16 mm and that of 4d were, apart from one specimen, around 20 mm displacement. It should be noted that a unit cell of the structure is a cube of side 16 mm, and each layer is one unit cell in height. The reloadings starting close to 16 mm in the 5d specimens indicate the crushing of the first layers. The slender struts and less stiff joints of the 4d specimens allow more even distribution of the compressive load within its layers, and thus explains the higher displacement corresponding to the troughs of force for the 4d specimens. In other words, the deformations localize earlier in 5d specimens but are more homogeneous in 4d specimens. Another evidence of homogeneous deformation in the layers of the 4d specimen is Figures 6 (a) and (b) where the 5d sample experienced a layer failure at 20% strain while the 4d specimen is intact and with better strain distribution in each layer. This also explains the slightly higher force at the troughs following layer failures in two 4d specimens, if the third specimen is considered an anomaly. After the first humps, the next two humps in both the configurations occur with an 11 mm deformation span although the humps in the 5d configuration have higher amplitudes, evidencing stress localization in the specimen boundaries close to the compression plate.

The collapse of a layer creates space within the structure, allowing it to expand and relieve some stress before reloading, and the cycle repeats. The troughs of force increasing gradually with each successive layer collapse in the 5d configuration can be partially attributed to debris from the failed layers contributing to progressive

densification and partially to the greater load sharing by the inner layers with each reloading. The densification effect is less significant in 4d specimens owing to their slender struts and the already higher deformation due to the load distribution within each layer in the primary failure, as already discussed. As a result, there is no increase in the trough forces with successive layer failures in the 4d specimens.

As the forces from the pentamodes reach their maximum values, plateaus around the maximum are observed. The plateaus are wider in the 4d configuration, suggesting a comparatively more ductile response than the 5d configuration. Failure invariably occurs at the layers on specimen boundaries adjacent to one plate or the other depending on the presence of defects for both configurations. This is due to the joints in those layers lacking reinforcement from either the top or bottom unlike the joints in the inner layers. Given that the structure is compromised in the proximity of the end where the layer failed first, successive layer failures continue from that end of the specimen.

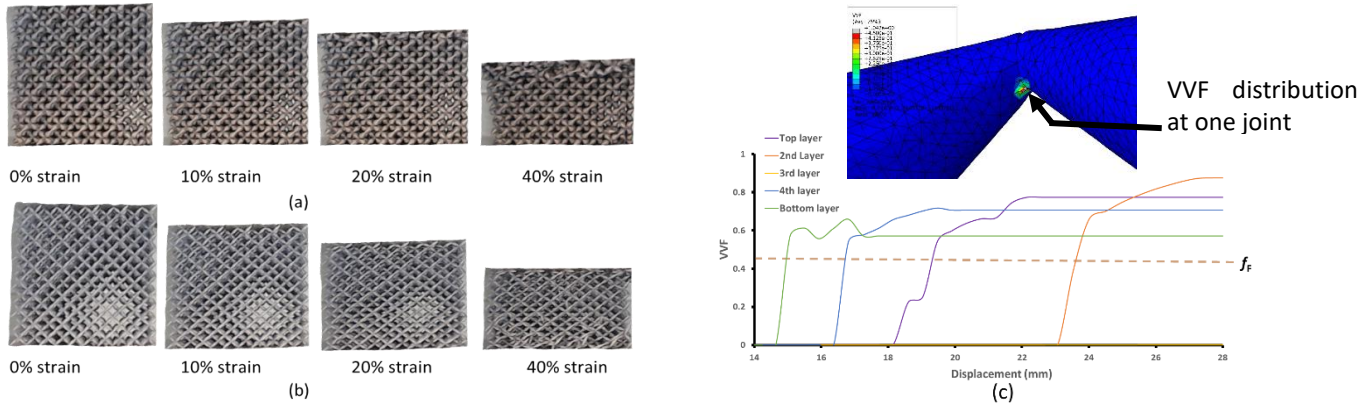


Figure 6. Deformation response of (a) 5d specimen and (b) 4d specimen at different strain stages (c) VVF at the corresponding nodes in the joints along a vertical line showing the order of joint integrity loss in numerical simulation of 4d configuration.

The numerical results, however, have a difference in the manner in which the joints approach failure. As observed in Figure 6(c), the joint on the bottom layer followed by the layer (4th layer) on top of it reaches the failing void volume fraction  $f_f$  first. The entire layer, however, does not collapse which is evident by the absence of any significant drop in the force-displacement curves in Figure 7 (a) and (b) for both pentamodes. The next nodes to reach  $f_f$  are in the top layer followed by the layer (2nd layer) under it. This confirms that failure begins at the specimen boundaries while the inner layer (3<sup>rd</sup> layer) remains intact. Although the VVF at a node in the joint shows  $f_f$  is surpassed in Figure 6(c), the entire joint does not fail as the contour indicates. This partly stems from the modelling simplifications which are unable to capture the microscale defects more common in complex part geometries like the strut joints due to inherent shortcomings of AM, and partly from model limitations, where material description that primarily captures ductile behavior (like the GTN model adapted for ductile metals), makes the model unable to predict brittle failure due to stress concentration [11] at the joints without modifications to model the AM manufactured polymers. Hence, crushing of the layers due to complete joint failures across an entire layer is not simulated, and load transfer to other layers nearer to both the compression plates (specimen boundaries) occurs, extending the plateau at maximum force in the numerical simulations as shown in Figure 7. Instances of force drop in FEA curves are identified with arrows in Figure 7 to show where the joints start failing and they correspond well with the first failures in the experiments. The GTN model of the damage region needs improvement to simulate the joint collapse more realistically.

The FEA results of the 5d configuration are within experimental bounds in the elastic and plastic region, but those of the 4d configuration are satisfactory to within the first 2 mm, after which they overestimate experimental results. The FEA models did not properly capture the damage region in either pentamodes.

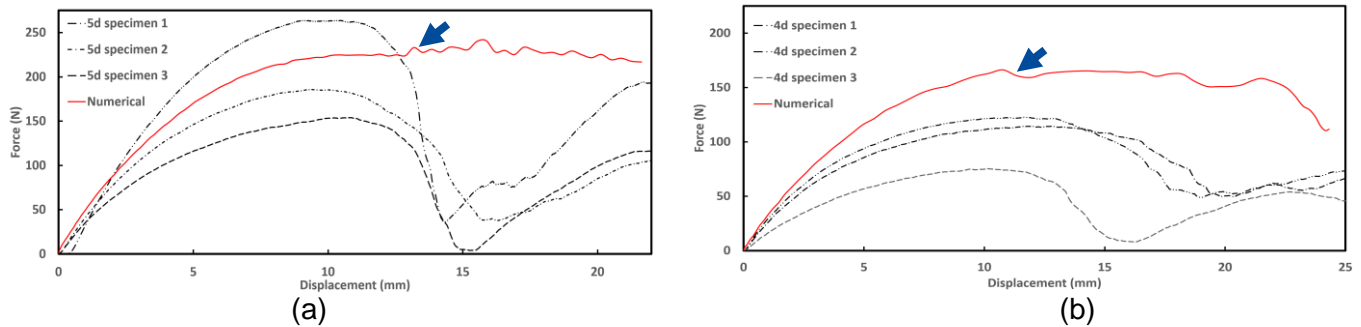


Figure 7. Comparison of numerical and experimental stress strain curves for pentamode compression of (a) 5d specimens, and (b) 4d specimens.

#### 4. Conclusion

A finite element (FE) model of pentamode structures is developed and validated against experimental results. Machine learning techniques effectively optimized the strain-hardening and damage parameters of tensile specimens. These optimized parameters were then successfully integrated into the FE model to simulate the response of the pentamode structures under compression. The FE results demonstrated good agreement with experimental data in the elastoplastic region; however, the model was less accurate in predicting the damage region. The initial results of this study should promote the development of more accurate predictive tool for 3D printed structures with complex geometries.

#### 5. References

- [1] J. Martín-Montal, J. Pernas-Sánchez, and D. Varas, "Experimental Characterization Framework for SLA Additive Manufacturing Materials," *Polymers*, vol. 13, no. 7, p. 1147, Apr. 2021, doi: 10.3390/polym13071147.
- [2] R. Hedayati *et al.*, "Analytical relationships for mechanical properties of pentamode metamaterials," preprint, Sep. 2023. doi: 10.31224/3239.
- [3] C. Le, K. Kolasangiani, P. Nayyeri, and H. Bougherara, "Experimental and numerical investigation of 3D-Printed bone plates under four-point bending load utilizing machine learning techniques," *Journal of the Mechanical Behavior of Biomedical Materials*, vol. 143, p. 105885, Jul. 2023, doi: 10.1016/j.jmbbm.2023.105885.
- [4] J. Dong, G. Ye, Y. Wang, F. Jin, and H. Fan, "Design, manufacture and crushing behaviors of buckling-inspired auxetic meta-lattice structures," *International Journal of Smart and Nano Materials*, vol. 12, no. 4, pp. 491–510, 2021.
- [5] M. Fu, Y. Chen, W. Zhang, and B. Zheng, "Experimental and numerical analysis of a novel three-dimensional auxetic metamaterial," *physica status solidi (b)*, vol. 253, no. 8, pp. 1565–1575, 2016.
- [6] X. Ren, J. Shen, P. Tran, T. D. Ngo, and Y. M. Xie, "Design and characterisation of a tuneable 3D buckling-induced auxetic metamaterial," *Materials & Design*, vol. 139, pp. 336–342, 2018.
- [7] X. Cheng *et al.*, "Design and mechanical characteristics of auxetic metamaterial with tunable stiffness," *International Journal of Mechanical Sciences*, vol. 223, p. 107286, 2022.
- [8] T. Webbe Kerekes, H. Lim, W. Y. Joe, and G. J. Yun, "Characterization of process–deformation/damage property relationship of fused deposition modeling (FDM) 3D-printed specimens," *Additive Manufacturing*, vol. 25, pp. 532–544, Jan. 2019, doi: 10.1016/j.addma.2018.11.008.
- [9] W. Jiang, Y. Li, and J. Su, "Modified GTN model for a broad range of stress states and application to ductile fracture," *European Journal of Mechanics - A/Solids*, vol. 57, pp. 132–148, May 2016, doi: 10.1016/j.euromechsol.2015.12.009.
- [10] D. W. Abueidda, M. Bakir, R. K. Abu Al-Rub, J. S. Bergström, N. A. Sobh, and I. Jasiuk, "Mechanical properties of 3D printed polymeric cellular materials with triply periodic minimal surface architectures," *Materials & Design*, vol. 122, pp. 255–267, May 2017, doi: 10.1016/j.matdes.2017.03.018.
- [11] H. Zhou, M. Zhao, Z. Ma, D. Z. Zhang, and G. Fu, "Sheet and network based functionally graded lattice structures manufactured by selective laser melting: Design, mechanical properties, and simulation," *International Journal of Mechanical Sciences*, vol. 175, p. 105480, Jun. 2020, doi: 10.1016/j.ijmecsci.2020.105480.